CHEMISTRY OF MATERIALS
Cite This: Chem. Mater. 2019, 31, 7510−7521
Article
pubs.acs.org/cm

Halogen-Induced Crystallinity and Size Tuning of Microwave Synthesized Germanium Nanocrystals

Katayoon Tabatabaei,[†] Alexandra L. Holmes,[†] Kathryn A. Newton,[†] Elayaraja Muthuswamy,[†] Roy Sfadia,[‡] Sue A. Carter,[‡] and Susan M. Kauzlarich*[,†]

[†]Department of Chemistry, University of California, One Shields Avenue, Davis, California 95616, United States
[‡]Department of Physics, University of California, Santa Cruz, California 95064, United States

Supporting Information

ABSTRACT: The reduction of Ge halides in oleylamine (OAm) provides a simple, yet effective high-yield synthetic route to germanium nanocrystals (NCs). Significant advances based on this approach include size control of Ge NCs, Bi doping of Ge NCs, and synthesis of $Ge_{1-x}Sn_x$ alloys. It has been shown that the size of Ge NCs can be controlled by the ratio of Ge^{2+}/Ge^{4+} in the reaction. Here, we show that finer control of absolute size and crystallinity can be achieved by the addition of molecular iodine (I_2) and bromine (Br_2) to germanium(II) iodide (GeI_2). We also show the presence of a Ge−amine−iodide complex and production of hydrogen and ammonia gases as side products of the reduction reaction. All reactions were carried out by microwave-assisted heating at 250 °C for 30 min. I_2 and Br_2 are shown to oxidize GeI_2 to GeI_4 in situ, providing good control over size and crystallinity. The kinetics of Br_2 oxidation of GeI_2 is slightly different, but both I_2 and Br_2 provide size control of the Ge NCs. The samples are highly crystalline as indicated by powder X-ray diffraction, selected area electron diffraction, transmission electron microscopy and Raman spectroscopy. Although both I_2 and Br_2 improve the crystallinity of the Ge NCs, I_2 provides overall higher crystallinity in the NCs compared to Br_2. Absorption (UV−vis−NIR) spectroscopy is consistent with quantum confinement for Ge NCs. The solutions of I_2, GeI_2, and colloidal Ge NCs were investigated with Fourier transform infrared and ^{1}H NMR spectroscopies and showed no evidence for imine or nitrile formation. The hydrogen on the amine in OAm is shifted downfield with increasing amounts of I_2, consistent with a more acidic ammonium species. Hydrogen and ammonia gases were detected after the reaction by gas chromatography and high-resolution mass spectrometry. The presence of a Ge−amine−iodide complex was also confirmed with no evidence for a hydrazine-like species. These results provide an efficient fine-tuning of size and crystallinity of Ge NCs using halogens in addition to the mixed-valence precursor synthetic protocol previously reported and demonstrate the formation of hydrogen as a reducing agent in OAm.

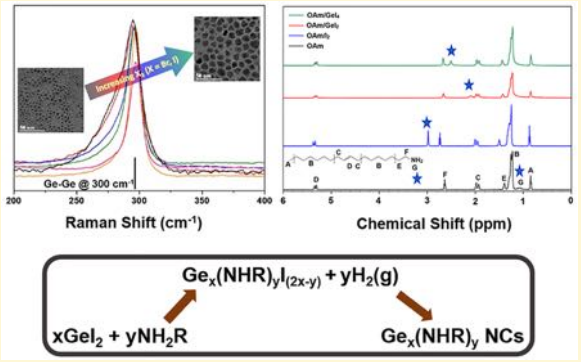

1. INTRODUCTION

Over the past 2 decades, colloidal synthesis has developed into a versatile and powerful method to create inorganic nanostructures. Solution-based synthetic methods have been able to deliver control over the nanocrystal (NC) size, shape, composition, and surface functionality with high precision for an ever-increasing range of materials.[1−3] Molecular halogens[4] and halide ions are shown by several research groups to have influence on the growth kinetics, morphology control, and surface functionalization of a variety of semiconductor,[5] metal NCs,[6] and perovskites.[7,8] For instance, chlorine has been used by Pietryga et al. to improve stability and the optical properties of PbSe NCs by etching out Se surface ions and forming a $PbCl_x$ thin layer on their surfaces.[4] An understanding of the chemical mechanism for the synthesis of Ge NCs is of significant importance. It would allow for the optimization and design of improved synthetic protocols that produce high-quality NCs with tunable size, morphology, composition, and surface characteristics.

Although significant advancements have been made in the empirical synthesis of germanium nanocrystals (Ge NCs), methods to reproducibly control size/morphology and a mechanistic understanding of growth are not as well developed as those of Cd- and Pb-based quantum dots. Robust synthetic methods for controlling size and surface passivation are required to advance their size- and shape-dependent properties for applications such as battery anodes[9,10] and optoelectronic devices.[11,12] With a narrow, bulk band gap of 0.67 eV (at 300 K), Ge is considered to be in the theoretical range of maximum efficiency for solar cells.[13] The Ge band gap combined with its large exciton Bohr radius ($a_0 \sim 24$ nm) allows for fine-tuning

Received: June 7, 2019
Revised: August 28, 2019
Published: August 29, 2019

DOI: 10.1021/acs.chemmater.9b02225
Chem. Mater. 2019, 31, 7510−7521

of the band gap over a broad range of NC sizes and allows the decoupling of thermal and electrical conductivity of these materials.[14] Recently, carrier multiplication was observed for Ge NCs with an average size of 5−6 nm illustrating their promise for applications in solar cells.[15]

Precise synthetic control over size, crystallinity, and surface is an ongoing challenge for Ge NCs, particularly due to the high crystallization temperature of Ge and its redox potential.[16,17] The reduction of GeI_2 and GeI_4 precursors in high boiling solvents to form Ge-based nanomaterials has been reported by a number of research groups.[18−23] These reactions demonstrate control over the size of Ge NCs, but the degree of crystallinity varies, depending on the temperature, the reducing agent, and the precursor (GeI_2 vs. GeI_4). Oleylamine (OAm) is commonly used as a solvent and electronic passivating ligand in the syntheses[24] of metal,[25] metal−halide perovskite,[26−28] and semiconductor[29−32] nanomaterials and is known as the "dominant coordinating solvent in the nanomaterial synthesis".[33−35] OAm was first identified as an effective reducing agent for GeI_2 by Wan and co-workers.[11] The primary amine has been demonstrated to play a critical role in the reaction; however, the detailed mechanism of the reduction reaction is not known.[36,37] Utilizing the novel size control strategy first reported by Neale and co-workers,[38] our group developed a microwave synthesis for the Ge NCs using OAm.[36] Although the synthesis resulted in crystalline nanoparticles at temperatures as low as 210 °C, the NCs were observed to suffer from incomplete surface passivation.[39] We have shown that OAm-capped Ge NCs have surface defects that can be detected by cyclic voltammetry and removed through hydrazine treatment and dodecanthiol (DDT) exchange.[39] The stability of the Ge NCs increases by exchanging the OAm ligands for DDT, and their size-dependent band gap was determined using surface photovoltage spectroscopy.[40] Recently, our group showed the nontrivial effect of a binary solvent system, comprised of OAm and 1-dodecene, on the size control and crystallinity of as-synthesized Ge NCs. When 1-dodecene is employed with OAm, it also binds to the surface of Ge. Increased amounts of 1-dodecene over that of OAm lead to larger NCs along with OAm/1-dodecene ratio-dependent mixed crystallinity of the Ge NCs.[23]

The ability to dope Ge NCs with a variety of main group elements utilizing halide precursors has also been demonstrated.[41] Doped materials are crucial for applications in devices where n- or p-type carriers are required. Recently, these synthetic methods have been extended to $Ge_{1-x}Sn_x$ alloy nanomaterials prepared from both metal halide and metal amide precursors.[42−44] The $Ge_{1-x}Sn_x$ alloying provides band gap engineering of the nanomaterial as a function of both size and composition. Although Ge is an indirect band gap material, the incorporation of Sn into the structure could lead to a quasi-direct or direct band gap, even for low compositions of Sn.[43] Additionally, there is a vast array of other Ge-based nanomaterials that could be developed with a better mechanistic understanding of their formation.

Hence, in efforts to provide better control of size and shape for Ge NCs and its alloys, the effect of halogens, I_2 and Br_2, on the production of Ge NCs from GeI_2 is systematically explored. Insight into the chemical reaction is obtained by using ^1H NMR and high-resolution mass spectrometry (HRMS) to probe the interaction of GeI_2 precursor in the presence of a primary alkylamine (OAm) and the contribution of I_2 to altering the basicity and, consequently, the chemical environment of the amine proton.

2. EXPERIMENTAL PROCEDURES

2.1. Chemicals. Oleylamine (OAm) (cis-9-octadecen-1-amine (CAS registry number 112-90-3)) was purchased from Sigma-Aldrich (>98% primary amine) and TCI America (>40% amine) and was used after degassing under reduced pressure at 150 °C for a minimum of 60 min. Germanium(II) iodide (GeI_2) was purchased from Prof. Richard Blair's laboratory (University of Central Florida)[45] and was characterized by powder X-ray diffraction (PXRD) to be phase-pure (Supporting Information (SI), Figure S1). Crystalline flakes of resublimed iodine were obtained from Johnson Matthey Chemicals Limited (Puratronic quality) and stored under an inert atmosphere. Bromine (99.5%) was obtained from STREM Chemicals. GeI_4, (99.999%) was purchased from STREM chemicals. Dioctylamine (DOA) (98%) and trioctylamine (TOA) (98%) were purchased from Sigma-Aldrich. Methanol, toluene, and acetonitrile were purchased from Fisher Scientific, purified using a commercial solvent purification system, and stored in a glovebox under argon.

2.2. Ge NCs Synthesis. All Ge NC syntheses were carried out in a Discover SP microwave reactor (CEM Corporation) in the dynamic mode unless otherwise specified. The microwave reactor is calibrated annually by a CEM technician and the measured temperatures are within ± 5 °C. A typical synthesis involves the addition of 0.40 mmol of GeI_2 (130.6 mg) into a 35 mL microwave reaction tube (purchased from CEM) followed by the addition of 8 mL (24.3 mmol) of degassed OAm using a calibrated pipet in an argon-filled glovebox. Calculated quantities of molecular I_2 or Br_2 are added to the microwave tube as needed (0.00 to 0.40 mmol). The contents of the microwave tube are sonicated in a water bath until complete dissolution of the precursor. The dissolution of GeI_2 results in a yellow-colored solution. I_2 or Br_2 also dissolves easily in OAm. Depending on the halogen concentration relative to GeI_2, a yellow to the almost colorless solution will form upon sonication. Typical reaction conditions involve heating the system for 30 min at 250 °C under the dynamic mode (set maximum power that oscillates to control the temperature). The dark brown product is isolated without exposure to ambient conditions by handling in a solvent box under an argon atmosphere. The NCs are isolated by centrifugation (8500 rpm) for 5−10 min with methanol as an antisolvent (the addition of antisolvent until turbidity point of the mixture) to remove the unassociated OAm molecules. The colorless supernatant is discarded, and the brown precipitate is dispersed in about 5 mL of toluene and is stored under argon for further characterization. For the control experiments, GeI_4/GeI_2 in molar ratios in the range of 0.0−1.0 (total Ge: 0.40 mmol) was added to 8 mL of degassed OAm in a 35 mL microwave tube. The dissolution of pure GeI_4 in OAm results in a colorless solution. The reaction and isolation procedures were similar to the aforementioned GeI_2/halogen protocol.

3. MATERIAL CHARACTERIZATION

Ge NCs and products from the reaction were characterized by powder X-ray diffraction (PXRD), transmission electron microscopy (TEM), scanning transmission electron microscopy (STEM), energy-dispersive X-ray spectroscopy (EDS), selected area electron diffraction (SAED), NMR spectroscopy, Raman spectroscopy, absorption (UV−vis−NIR and Fourier transform infrared (FTIR)) spectroscopies, high-resolution mass spectrometry (HRMS), and gas chromatography (GC).

3.1. Powder X-ray Diffraction (PXRD). Powder X-ray diffraction (PXRD) patterns were collected by drop-casting the dispersion of Ge NCs in toluene onto a quartz substrate or silicon (Si_{510}) single-crystal zero-background holder. Solvent evaporation results in a dark brown-colored thin film of the NCs that was then scanned on a Bruker D8 Advance diffractometer (Cu Kα, 40 kV, 40 mA). The step size of the

DOI: 10.1021/acs.chemmater.9b02225
Chem. Mater. 2019, 31, 7510−7521

measurement was 0.02° in the 2θ range of 20−75°. The obtained data were compared to the (04-0545—diamond cubic Ge) Powder Diffraction File from the International Center for Diffraction Data database. To estimate the crystallite size of the NCs, the Scherrer method has been carried out by fitting (pseudo-Voigt) the (220) reflection applying the Jade 6.0 software.

3.2. Transmission and Scanning Transmission Electron Microscopy (TEM/STEM). Samples for both TEM/STEM were prepared by drop-casting the dilute dispersion of Ge NCs in toluene onto either lacey carbon supported by a 400 mesh copper grid (Ted Pella) or a holey carbon film supported by a 300 mesh copper specimen grid (SPI). The grids were dried completely under an incandescent light or in an oven overnight to avoid carbon contamination of the vacuum chamber during electron beam irradiation. The TEM imaging and selected area electron diffraction (SAED) of the samples were performed using a JEOL JEM 2500SE transmission electron microscope (JEOL Ltd. Tokyo, Japan). The instrument is operated at 200 keV and is equipped with a Schottky field-emission electron gun (FEG) and a retractable 1 k × 1 k Gatan Multiscan CCD camera (model 794). NCs obtained from GeI_2/GeI_4 reactions were imaged at 200 keV in the STEM mode with an aberration-corrected JEOL JEM-2100F/Cs STEM equipped with Gatan annular dark-field (ADF) and STEM bright-field detectors. For STEM imaging, the electron probe convergence semiangle was approximately 23 mrad and the ADF inner detector semiangle was 33 mrad, hence resulting in medium angle annular dark-field contrast for which some diffraction contrast cannot be neglected. Both bright- and dark-field micrographs were collected. The DigitalMicrograph software provided by Gatan Inc. was used to collect images. To determine the average particle size and respective standard deviation, 150−250 individual NCs were imaged from different sample areas and multiple specimen grids. Particle sizes were calculated from intensity line profiles across individual particles in one consistent direction using the Image J software package. Energy-dispersive X-ray spectroscopy mapping (EDS) of the samples was carried out using a Thermo Corporation EDS spectrometer attached to the JEOL JEM 2500SE.

3.3. Raman Spectroscopy. Raman spectra were collected using a Renishaw RM1000 laser Raman microscope (514 nm) with a motorized stage. Samples were prepared by drop drying a concentrated solution of Ge NCs in toluene on the Al foil or Si substrate. To ensure reproducibility, different areas of the sample were scanned. Experimental data were analyzed using the Mathematica 11.0.1.0 software.[46] Experimental spectra from 100 to 1000 cm^{-1} were fit as the sum of two Lorentzian functions and a baseline function to obtain the peak position and full width at half maximum (FWHM), using the following equation

$$F(x) = \frac{A_1 \Delta f_1^2}{4\left[(f_1 - x)^2 + \left(\frac{\Delta f_1}{2}\right)^2\right]} + \frac{A_2 \Delta f_2^2}{4\left[(f_2 - x)^2 + \left(\frac{\Delta f_2}{2}\right)^2\right]} + \text{base} \quad (1)$$

where A_n is the peak height, Δf_n is the full width at half maximum (FWHM), f_n is the peak center, and x is the Raman shift in wavenumbers. The base constant compensates for the background intensity off-set.

The analysis of the Raman peaks with the phonon confinement model employed for Ge nanocrystals was also investigated. The dispersion relation was employed,

$$\omega(q_r) = \sqrt{\left[\omega_0^2 - 43565 \frac{q_r^2}{\{|q_r| + 0.5766\}}\right]} \quad (2)$$

where $\omega(0)$ is the Raman peak position of bulk Ge at room temperature (301 cm^{-1}), q_r is the reduced wave vector with $q = (2\pi/a)q_r$, and a is the lattice parameter of Ge (0.566 nm).[47,48] Ge powder (100 mesh, 99.999% metals basis, Alfa Aesar) was measured as a standard with the Ge−Ge optical phonon at 301 cm^{-1} and FWHM of 10 cm^{-1}.

3.4. UV−vis−NIR Spectroscopy. Spectra of diluted toluene dispersions of the OAm-capped Ge NCs were obtained at room temperature on a UV-3600 Plus Shimadzu UV−vis−NIR spectrophotometer, using an optically transparent quartz cuvette with an optical path length of 1 cm. The spectra were recorded in the range of 300−1600 nm in a dual beam mode at a medium scan rate and 1.0 nm wavelength interval. The spectrum of the background absorption of the same solvent (toluene) was subtracted from the sample absorption.

3.5. FTIR Spectroscopy. FTIR measurements were carried out with a Bruker Alpha spectrometer. Toluene dispersion of samples was dispensed directly onto the attenuated total reflection-crystal and allowed to air dry.

3.6. NMR Spectroscopy. Samples for ^1H and ^{13}C NMR were prepared by evaporating toluene dispersions of Ge NCs in a vacuum oven at 60 °C and dissolving them in the $CDCl_3$ solvent under an inert atmosphere. ^1H and ^{13}C NMR spectra were obtained at room temperature on a 400 MHz Bruker Advance IIIHD Nanobay Spectrometer or 600 MHz Varian VNMRS spectrometer. Chemical shifts were referenced to residual undeuterated $CHCl_3$ (7.26 ppm).

3.7. High-Resolution Mass Spectrometry (HRMS) and Gas Chromatography (GC). For high-resolution mass spectrometry (HRMS), dilute toluene dispersions of Ge NCs were analyzed by flow-injection analysis into a Thermo Fisher Scientific LTQ Orbitrap (San Jose, CA) operated in the centroid mode. Samples were injected into a mixture of 50% methanol and 0.1% formic acid/H_2O at a flow of 200 μL/min. Source parameters were 5.5 kV spray voltage, the capillary temperature of 275 °C, and sheath gas setting of 20. Spectral data were acquired at a resolution setting of 100,000 FWHM with the lock mass feature, which typically results in a mass accuracy <2 ppm.

Qualitative measurement of hydrogen and ammonia gases was performed on a Varian 3800 GC equipped with a thermal conductivity detector and a Carboxen 1010 PLOT fused silica column (30 m × 0.53 mm) (Supelco) using nitrogen (99.999%, Praxair) as the carrier gas. The GC spectra are plotted using the plot digitizer software to convert a screenshot of the spectra (very old GC computer) to the plots of the scans.

4. RESULTS AND DISCUSSION

4.1. Nanocrystal Synthesis and Characterization. Microwave-assisted synthesis of Ge NCs using GeI_2 or mixed valent GeI_2/GeI_4 as Ge precursors in OAm under air-free environment was previously developed.[36] The work presented here shows the synthesis of nanocrystals of Ge by the microwave-assisted reaction of GeI_2 using halogens (either Br_2

DOI: 10.1021/acs.chemmater.9b02225
Chem. Mater. 2019, 31, 7510−7521

or I_2) in OAm. OAm (cis-$CH_3(CH_2)_7CH{=}CH(CH_2)_8NH_2$), a primary unsaturated amine, is a common solvent and coordinating ligand in the synthesis of nanomaterials.[25,29−32,49−53] OAm is a liquid at room temperature (T_m ~ 20 °C) and has a high boiling point (~350 °C); these two attributes allow for facile isolation of NCs and the ability to tune the reaction over a wide range of temperatures. In addition to its solvent role, OAm can act as an electronic passivating ligand, long-chain surfactant stabilizing NCs colloids, and mild reducing agent.[50,51,54]

OAm can be purchased with different grades of purity (40−98% in primary amine content). As previously reported in the literature,[55] the $[CH_2]$:$[NH_2]$ ratio for 40% OAm is higher, attributed to the presence of heavier hydrocarbons, compared to 70−98% primary amine content. In this work, we initially used 98% OAm for GC and NMR studies to avoid hydrocarbon impurities that might be present in technical grade OAm. Since no noticeable difference in microwave heating of products was observed under consistent reaction conditions, we employed 40% OAm for the majority of the Ge NCs syntheses. The reagents in our reaction are the major contributors to how rapidly the solution reaches the set temperature since OAm does not efficiently absorb microwaves. In addition, we run the reaction under the dynamic mode (automatic power); as the microwave reactor approaches the desired temperature, the instrument oscillates the microwave frequency on and off to not surpass the desired temperature. Any material containing mobile electric charges, such as polar molecules or conducting ions in a solvent or solid, can be heated by means of microwaves. The reagents can absorb microwaves at a given frequency and temperature because of the value of the loss tangent, which is the tangent of the ratio of the dielectric loss divided by the dielectric constant. The dielectric loss provides the conversion efficiency of the electromagnetic radiation into heat, and the dielectric constant corresponds to the polarizability of the molecule in the electric field.[56−59] GeI_2 has been shown to be a good microwave absorber.[36] In this study, the halogen is always mixed with GeI_2 in OAm and provides additional absorption of microwaves that translate into faster heating of the solution. The effect on microwave heating rates of increasing the concentration of each halogen, Br_2 or I_2, compared to the reaction of GeI_2 with no added halogen is shown in Figure 1. The individual heating profiles for each concentration of halogen are shown in the Supporting Information (SI, Figure S2). I_2 increases the microwave heating rate relative to that of Br_2.

Figure 1a displays the time required to reach 250 °C for varying concentrations of Br_2 and I_2 (for 0.40 mmol GeI_2 in OAm) and shows that both I_2 and Br_2 increase the heating rate of the solution compared to GeI_2 (black solid line) by itself. The plot of time to reach 200 °C provides a more quantitative evaluation of the effect of the halogen on the ramp rate and consistently shows that iodine containing solutions reach temperature faster. These results suggest that these halogens are forming molecular or ionic species in the solution that lead to better absorption of microwaves.[56,60−62] The exact mechanism of heat transfer with microwaves for halogens in nonabsorbing liquids has not been elucidated, but it can be speculated that various polar or ionic species can arise such as H^+X^- or $RNH_3^+X^-$.

In all reactions, the GeI_2 precursor was held constant at 0.40 mmol (consistent with previous experiments),[36] and only the halogen concentration was varied. PXRD characterization of

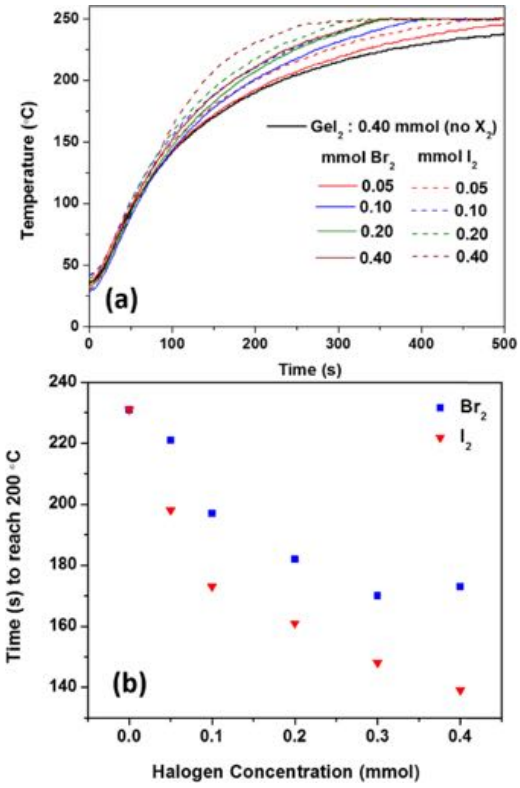

Figure 1. (a) Temperature profiles for microwave heating of reactions comprising of constant 0.40 mmol GeI_2 and varying quantities of I_2 or Br_2 (0.00, 0.05, 0.10, 0.20, and 0.40 mmol) in 8 mL (24.3 mmol) of OAm (X_2 stands for halogen). (b) Time required to reach 200 °C versus halogen amount (0.00, 0.05, 0.10, 0.20, 0.30, and 0.40 mmol) added to 0.40 mmol GeI_2 in 8 mL (24.3 mmol) of OAm.

reactions of GeI_2 with with 0.00 to 0.40 mmol halogen 0.00 to 0.40 mmol halogen indicates the formation of phase-pure cubic Ge (Figure 2). The observed diffraction signals at 27.3, 45.4, and 54.5° are assigned to the (111), (220), and (311) lattice planes of diamond cubic Ge, respectively. The crystallite size was determined from the broadening of the (220) reflection based on the Scherrer analysis.[63] The (111) reflection was not used to reduce errors from peak asymmetry and background removal. Scherrer's formula is shown as eq 3. Crystallite size, L, is proportional to X-ray wavelength in nm (λ) and crystallite shape (constant K proportionality factor, normally considered as 0.94 for spherical crystals with cubic symmetry) and is inversely proportional to angle (θ) and the width of the diffraction peak at half maximum height (β in radian). Crystallite size increased gradually from 3.3 to 18 nm as the quantity of halogen increased (Table 1). Previous work has demonstrated a similar size relationship for GeI_2/GeI_4 reactions run under similar conditions.[36,38] The PXRD patterns of Ge NCs obtained from GeI_2/GeI_4 as control reactions are shown in the Supporting Information (Figure S3 and Table S1).

$$L = \frac{K\lambda}{\beta \cos\theta} \tag{3}$$

The TEM images (Figures 3 and 4) indicate the formation of quasi-spherical NCs. The morphology of NCs is consistent with that obtained in our previous work using GeI_2 and GeI_4 at lower reaction temperatures.[36] The size distribution histograms are calculated for each image. Consistent with the

DOI: 10.1021/acs.chemmater.9b02225
Chem. Mater. 2019, 31, 7510−7521

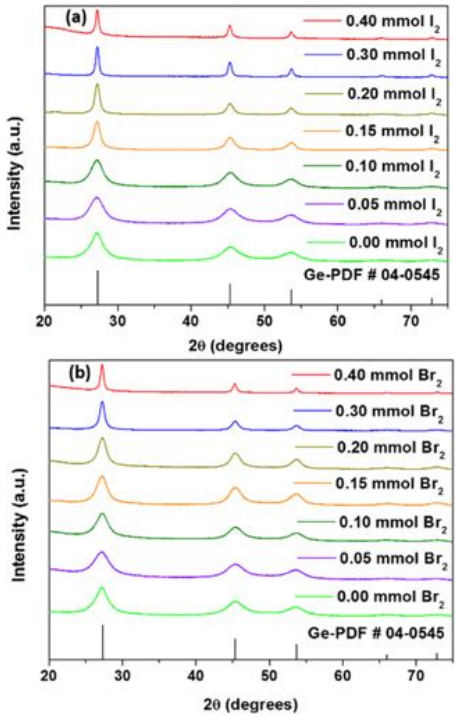

Figure 2. PXRD patterns of Ge NCs prepared with varying quantities of (a) I_2 and (b) Br_2 compared to the reference pattern (PDF #04-0545) showing the (111), (220), (311), (400), and (331) reflections of cubic Ge.

Table 1. Summary of Crystallite Size for OAm-Capped Ge NCs Obtained from the Reaction with Constant 0.40 mmol GeI_2 Precursor and Increasing Amounts of Halogen or GeI_4 (for GeI_2/GeI_4 Reactions, Total Ge Content is Held 0.4 mmol) in OAm at 250 °C

	crystallite size (nm)[a]		
mmol halogen	I_2	Br_2	GeI_4
0.00	3.1 ± 0.10	3.1 ± 0.10	3.1 ± 0.10
0.05	3.4 ± 0.10	3.3 ± 0.10	3.4 ± 0.10
0.10	4.0 ± 0.10	4.1 ± 0.10	4.7 ± 0.10
0.15	6.6 ± 0.10	4.7 ± 0.10	9.1 ± 0.10
0.20	8.7 ± 0.10	5.6 ± 0.10	11.7 ± 0.10
0.30	16.8 ± 0.20	8.7 ± 0.10	ND
0.40	17.7 ± 0.20	17.2 ± 0.20	ND

[a]Based on the Scherrer method employing the (220) reflection.

average crystallite size obtained from PXRD patterns, the TEM images indicate a gradual increase in NC size with the increasing quantity of I_2 and Br_2 (Figures 3 and 4), with size distributions in the range of 13−20%. The sizes obtained from TEM images were consistently found to be larger than the crystallite sizes reported in Table 1. The Scherrer equation has the tendency to underestimate the actual size of the NCs.[64] The differences may be attributed to amorphous character of the surface and the fact that PXRD is sampling a significantly larger amount of the material than TEM.[64] The crystallite size tunability achieved via oxidation by I_2 (Ge^{2+}/Ge^{4+}) is in the range 4−20 nm. Although the uniform distribution of individual NCs is observed for NCs up to 10 nm in diameter, the larger NCs are present as agglomerates on the TEM grid and do not form stable colloidal solutions (Supporting Information, Figures S4 and S5). The histograms of Ge NCs

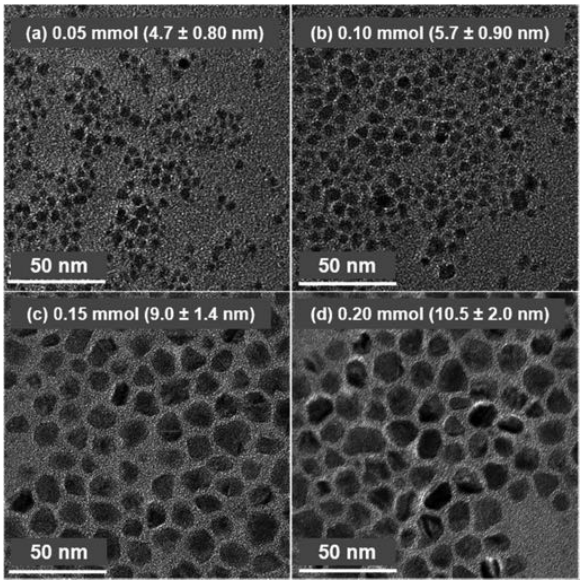

Figure 3. Size and morphology: TEM images of Ge NCs prepared with 0.40 mmol and varying quantities of I_2 (0.05−0.20 mmol). The average size with the standard deviation is provided along with iodine quantity at the top of each image.

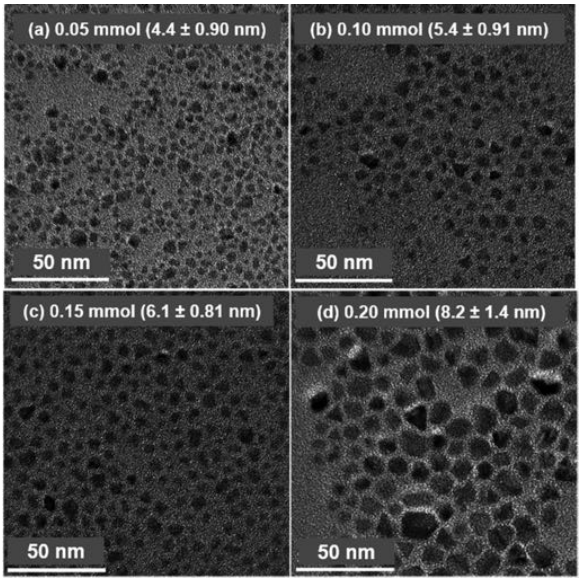

Figure 4. Size and morphology: TEM images of Ge NCs prepared with 0.40 mmol and varying quantities of Br_2 (0.05−0.20 mmol). The average size with the standard deviation is provided along with iodine quantity at the top of each image.

diameters and their fit to a Gaussian model are provided in the Supporting Information (Figures S6 and S7).

Selected area electron diffraction patterns obtained from OAm-capped Ge NCs synthesized in the presence of halogens clearly show the crystalline diamond cubic structure of Ge and increased crystallinity with higher halogen concentration (SI, Figures S8 and S9). The corresponding diffused ringlike SAED patterns confirm the polycrystalline nature of Ge NCs. The measured lattice constant of 3.2 Å is consistent with a lattice spacing of diamond cubic Ge (111) reflection.[11,18]

Energy-dispersive X-Ray spectroscopy (SI, Figures S10 and S11) was performed to confirm the NC composition, and Ge, C, O, and Cu are clearly distinguished. The C and Cu peaks

DOI: 10.1021/acs.chemmater.9b02225
Chem. Mater. 2019, 31, 7510−7521

are due to the holey and Lacey-carbon TEM grids used to support the samples. The oxygen signal is attributed to the oxidation of Ge NCs from the TEM grid preparation.

To validate in situ formation of GeI_4, we qualitatively compared the color of the starting mixture (SI, Figure S12). GeI_4 and GeI_2 in OAm are colorless and yellow, respectively. The addition of I_2 to GeI_2 in OAm reduces the color to an almost colorless solution when the ratio of GeI_2/I_2 increases from 1:0 to 1:1. Surpassing the stoichiometric amount of I_2 to oxidize all GeI_2 to GeI_4 results in a reddish solution attributed to the excess of I_2 in OAm. Additionally, we compared the crystallite sizes of NCs reported in Table 1 with the sizes obtained for NCs prepared by the direct addition of GeI_4. The GeI_2/GeI_4 reactions were carried out at constant Ge concentration under identical conditions (250 °C, 30 min). A plot of quantity of the reagent (I_2 or GeI_4) added to GeI_2 precursor versus NC size reveals that the effect of I_2 on NC size is similar to that of GeI_4 for lower concentrations; however, it shows a more dramatic enhancement for higher GeI_4 concentrations compared to identical concentrations of I_2 (Figure 5).

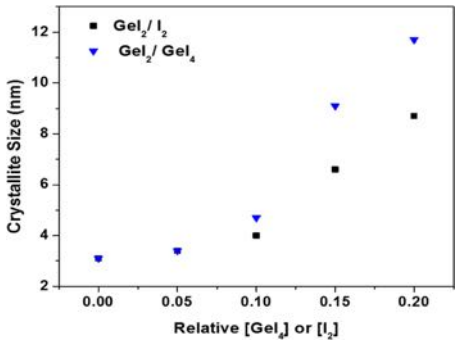

Figure 5. Comparison of the crystallite size of Ge NCs obtained from two different reaction methods: GeI_2/GeI_4 (blue triangle) and GeI_2/I_2 (black square).

The TEM images of Ge NCs prepared by control reactions of GeI_2/GeI_4 and their corresponding histograms are shown in the Supporting Information, Figure S13. A plot of particle size versus relative amounts of GeI_4 or I_2, provided in the Supporting Information, Figure S14, displays a similar trend. The smaller Ge NCs sizes at higher I_2 concentration compared to GeI_4 may be attributed to the faster microwave heating rate in the case of I_2 and enhanced nucleation kinetics (SI, Figure S15).

The crystallinity and successful reduction of GeI_2 to elemental Ge for the Ge NCs was investigated with Raman spectroscopy (Figures 6 and S16). The Ge−Ge optical phonon for bulk Ge occurs at ∼300 cm^{-1}.[65−67] A peak at about 300 cm^{-1}, consistent with crystalline Ge, is observed, and an amorphous Ge peak, expected at 154 and 274−280 cm^{-1}, is not observed.[68−73] There is no evidence for any form of GeO_2.[74] The Raman spectra of the smaller sizes show significant asymmetry in the peak on the low wavelength side. Peak broadening and shifts to lower energy are known to occur for nanomaterials due to quantum confinement size effects and strain at the surface, particularly for covalently bonded materials.[75,76] These effects have also been shown in the case of Si NCs with different surface terminations.[77] To quantify peak wavelength shifts and broadening, each spectrum was fit with the sum of two Lorentzian functions and a baseline

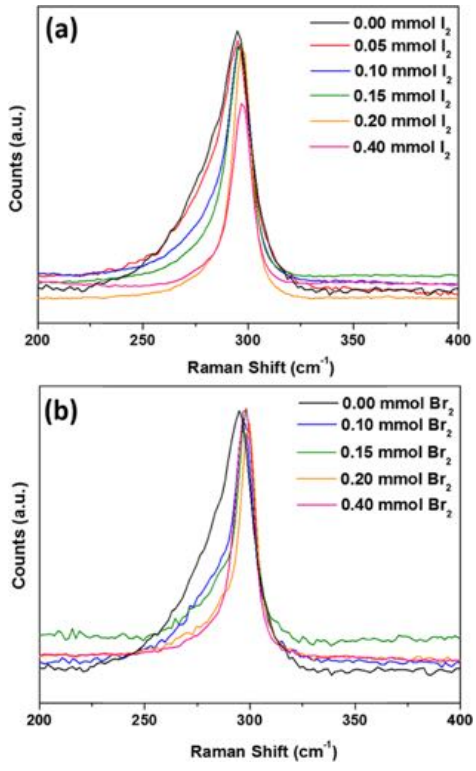

Figure 6. (a) Raman spectra of Ge NCs synthesized from GeI_2 with varying I_2 concentrations (0.0−0.04 mmol). (b) Raman spectra of Ge NCs synthesized from GeI_2 with varying Br_2 concentrations (0.0−0.40 mmol). As the amount of halogen added to the reaction increases, there is an increase in the particle size and crystallinity.

function (SI, Figures S17−S19 and Table S2).[78,79] The higher frequency peak is the Ge−Ge phonon mode (Lorentz 1), representative of the crystalline character of the NCs, and the shift is attributed to quantum confinement. The anisotropy at a lower frequency (Lorentz 2) is attributed to quantum confinement, disorder, and surface bonding and is significant for crystallite sizes less than 10 nm. The experimental Raman shift and the full width at half maximum (FWHM) of the optical phonon and asymmetry peaks of the various samples have inverse trends, with the FWHM of the peaks decreasing with the increasing crystallite size (Figure 7). Narrowing of the main peak of the Ge−Ge optical phonon mode is consistent with increasing crystallinity and size. No secondary phases attributed to the strong and Raman active covalent Ge−N interaction were detected.[80,81] The low-frequency tail can be calculated using the phonon confinement model,[47,48] which should account for the peak position and width for particles less than 10 nm. Comparing the peak shift according to an improved phonon confinement model by Volodin,[76] we find good agreement with the crystallite size of about 3 nm. Above 4 nm, there is a deviation of the shift from that projected from the model. The asymmetry and the width of the Raman peak were not well modeled, with the model underestimating the asymmetry and overestimating the width.

A simpler form of the phonon confinement model that has been used for the Raman spectra of Ge NPs embedded in silica[47] was employed to determine whether the experimental data could be better modeled. Similar to the Volodin model, we find that the optical phonon peak shift does not agree well with our experimental data for crystallite or particle diameters less than 4 nm but is reasonable for larger sized particles and

DOI: 10.1021/acs.chemmater.9b02225
Chem. Mater. 2019, 31, 7510−7521

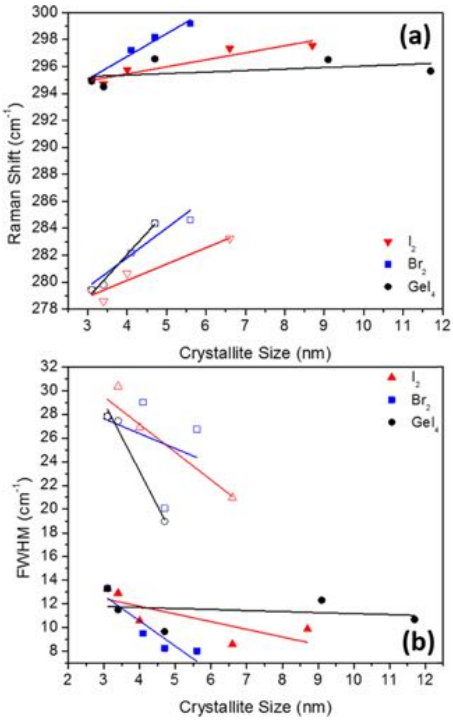

Figure 7. (a) Raman Shift (cm^{-1}) and (b) full width at half maximum (FWHM) as a function of the crystallite size for NCs synthesized with varying quantities of I_2, Br_2, and GeI_4. The closed and open symbols correspond to fitting the crystalline Ge−Ge optical phonon (Lorentz 1) and the asymmetry (Lorentz 2) peaks, respectively.

that the asymmetry is underestimated (see the SI, Figure S20). The low-frequency tail has been interpreted as arising from changes in the bond length (small particles have a higher surface to volume ratio and, therefore, a larger fraction of uncoordinated surface atoms with shorter bond lengths).[77] This induces Raman scattering at lower frequencies and that is a major component of the tail. With increasing NC size, the tail shifts to higher frequencies and its intensity decreases. This interpretation is consistent with the data presented.

Figure 8 shows the peak areas of the optical phonon vs asymmetry component of the Raman spectra from Ge NCs synthesized using halogen or GeI_4 under the same reaction conditions (SI, Table S2). In general, the percentage of total peak area from the optical phonon peak increases with the

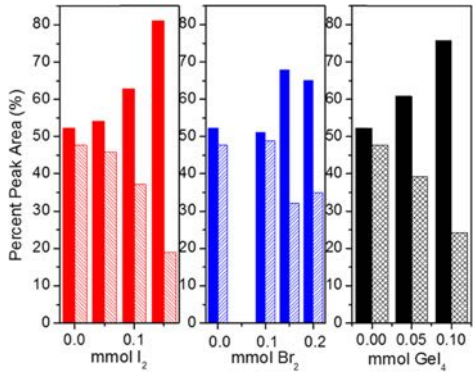

Figure 8. Percent peak area of the crystalline Ge−Ge optical phonon (filled) and asymmetric (hashed) peaks as a function of the amount of (a) I_2, (b) Br_2, or (c) GeI_4 added to the reaction.

particle size consistent with the increasing crystallinity. The graphs show that both I_2 and GeI_4 provide an increasing optical phonon peak area compared to the asymmetric component as a function of concentration. At 0.1 mmol of I_2 and GeI_4 precursors, the Ge NCs crystallite sizes are 4.0 nm vs 4.7 nm, respectively; the crystallite size is controlled by the microwave (MW) heating rate. As mentioned above, the faster heating rate gives rise to smaller particles in the case of I_2. This could be the result of localized superheating due to the enhanced absorption of I_2 in the MW. Similar to the reactions of GeI_2 and GeI_4, the reaction ramp rate to 250 °C was dependent on the amount of I_2 and Br_2 added to the reaction, which indicates that the MW absorption efficiency of the solution is increasing.[36] The trend of increasing area of the optical phonon mode is not consistent for the Br_2 reactions, which is attributed to Br_2 having a lower MW absorption efficiency and a slower reaction ramp rate.

The absorbance measurements were carried out in the range of 300−1600 nm with dilute dispersions of the Ge NCs in toluene. The plots for GeI_2/I_2 reactions are shown here (Figure 9a) and for GeI_2/Br_2 and GeI_2/GeI_4 are shown in the

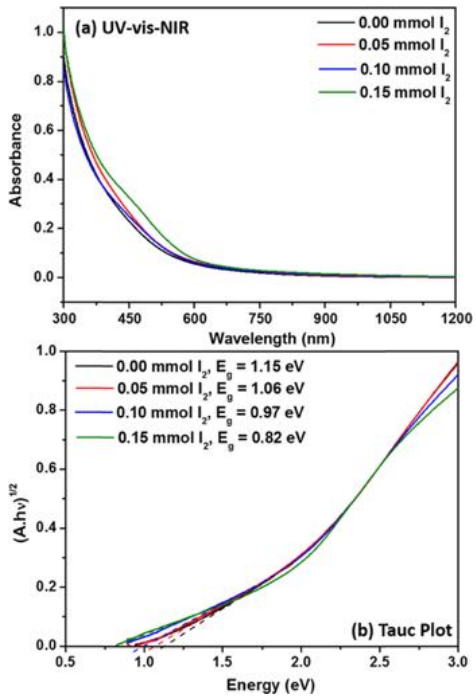

Figure 9. Optical Characterization: (a) UV−vis−NIR spectra of Ge NCs prepared with 0.40 mmol GeI_2 and varying quantities of I_2 dispersed in toluene and (b) Tauc plot of the absorption spectra. Extrapolation of the curve is shown with dashed lines.

SI, Figures S21a and S22a. The absorption spectra are characterized by a featureless trace until approximately 600 nm. This is consistent with expectations for an indirect band gap semiconductor. A red shift in the absorption trace from 300 to 600 nm can be observed with increasing NC size. Similar responses have been previously reported for Ge NCs.[38,40] Tauc plots (Figures 9b, S21b and S22b) were obtained by plotting the square root of the product of absorbance times energy versus energy. The plot provides an estimation of the band gap extracted from the onset of the curve. The band gap values extracted from Figure 9b range from 1.15 eV (0.0 mmol I_2) to 0.82 eV (0.15 mmol I_2) for the

DOI: 10.1021/acs.chemmater.9b02225
Chem. Mater. 2019, 31, 7510−7521

smallest and larger NCs, respectively. The trend obtained for the band gap values is consistent with the expected quantum confinement effects in NCs, however these absorption spectra were not corrected for light scattering. Light scattering would be more pronounced for larger particles and makes it difficult to determine the absorption onset.

4.2. Understanding the Role of OAm and I_2. The generally accepted mechanism for the synthesis of Ge NCs in OAm is that at sufficient temperature there is enough reducing power in OAm to reduce Ge halides to Ge NCs.[11] If one considers the simple correlation of NC size to the reducing ability of the reagent, then increasing the size of NCs with increasing halogen could be interpreted as attenuating the reducing power of the OAm solution and thereby leading to fewer nucleation events.[51,55] The complication of both a reducing solvent and oxidizing halogen reagent makes it difficult to deconvolute the competing effects, but at low concentrations, the halogens act in a similar fashion as GeI_4 and control size. In addition, the halogens allow for a finer control of size than that obtained by employing GeI_4.

Alkylamides $M(NR_2)_n$ are known to be suitable precursors to obtain different types of nanomaterials due to the high reactivity of single-element nitrogen bonds and facile reduction of those materials attributed to the polar M−N bond.[82] Organoamines are typical passivating ligands for NCs owing to the coordination of the nitrogen head group with the surface atoms of the NCs.[83,84] OAm is often chosen as an inexpensive and commercially available solvent for the synthesis of colloidal semiconductor NCs because it solubilizes both inorganic and organometallic precursors, is a mild reducing agent, and has a high boiling point (bp ≈ 350 °C). It has been reported that OAm can contribute as an electron donor at high temperatures.[49] Other high boiling amines, such as dioctylamine (bp ≈ 297 °C) and trioctylamine (bp ≈ 366 °C), were investigated for the reaction. Dioctylamine (DOA) is able to reduce GeI_2 under the reaction conditions used here (MW heating at 250 °C for 30 min); however, even at elevated temperatures, trioctylamine (TOA) is unsuccessful at producing Ge NCs. Previous results confirmed the amine to be crucial and ruled out the carbon−carbon double bond as a contributor in the reaction,[36,85] but the inability of a tertiary amine to reduce the Ge halide precursor suggests that a proton from the amine has a crucial role in the mechanism of NC formation.

Given that redox chemistry occurs in the reaction, there are several viable pathways for NC formation. Chen et al. have proposed that for the reduction of Ag^+ to form Ag nanoparticles, OAm is oxidized to either an imine or a nitrile, based on FTIR characterization, and is mediated by Ag^+.[51] Mishra et al. also reported observing a very weak band at 2172 cm^{-1} attributing to the formation of nitrile species during the formation of Ag and Au NPs using hexadecylamine as the reducing agent and capping ligand.[86] They correlated the blue shift of the observed nitrile band to the end-on coordination of the nitrile group to the metal atoms. There is evidence for neither imine, nor nitriles, by FTIR or NMR in our work (see below and Figure S23). In the FTIR spectra shown in the Supporting Information, bands around 3005, 1630, 1065, and 966 cm^{-1} correspond to the stretching vibration of =C−H, scissoring of NH_2, bending of NH_2, and trans =C−H in-plane and out-of-plane wagging, respectively (it was reported that the OAm can undergo cis−trans isomerization during its synthesis and as-received OAm contains trans isomer up to 43%).[87] Neither the stretching band of C≡N (2240−2260 cm^{-1}), the stretching vibration of =N−H (3300 cm^{-1}), the C=N vibration (1660 cm^{-1}) nor the =N−H deformation vibration (1580 cm^{-1}) is observed.[88,89] Additionally, previous NMR studies of Ge NCs do not show imine or nitrile donation to the NC surface, although it should be noted that NMR is not a sensitive enough characterization technique to detect trace amounts of such species.[39]

Thermodynamically favorable formation of 1:1 complexes by the mixture of the dilute solutions of iodine and amine in nonpolar solvents has been known for a long time, and the resulting turbid solutions are indicative of ionic species formation.[90−93] When solely considering the interaction between amines and I_2, the primary amine could be oxidized by I_2 to form iodoamines (RNHI) and in the presence of an excess of amines, could form air-sensitive substituted hydrazine complexes, which can also act as reducing agents.[94−98] Control experiments, in which OAm is either mixed or heated under MW reaction conditions with I_2, do not show evidence for substituted hydrazine formation. Iodine is considered to act as a Lewis acid catalyst in these reactions. For the interaction of I_2 as a Lewis acid with primary amines (N sp^3) as a Lewis base, the average pK_{bI2} was determined to be 3.0.[99] By comparison, the pK_b for octadecylamine (similar C18 chain primary amine, but saturated) is determined to be 3.4.[100] The solution becomes less basic upon the addition of I_2, rendering it a less reducing environment attributed to increased positive oxidation potential of the solution. The addition of molecular iodine attenuates the growth kinetics of the Ge NPs consequently. The iodide ion (I^-) is large and polarizable, resulting in an increase in nucleophilicty in protic solvents, and its reactivity is characterized by its weak basicity and ability to be a good leaving group.

To confirm that the addition of I_2 is necessary, ammonium iodide (NH_4I) or sodium iodide (NaI) was added to the reactions. Both iodide sources had no effect on the NC size when MW was heated in OAm with GeI_2. The formation of the ammonium iodide salts as a product is important for the reaction to proceed. The presence of Ge−amine−iodide complexes was confirmed by high-resolution mass spectrometry (HRMS). The mass spectra and determined fragments are shown in the Supporting Information (Figure S24 and Table S3). The peak with the mass of 518.5638 m/z is attributed to the dimerization of OAm and the loss of one ammonia molecule. A peak with the exact mass of 772.3673 amu corresponds to a Ge−amine−iodide complex (Ge $(OAm)_2I$). Gas chromatography (GC) was used to qualitatively determine the environment in the headspace of the MW tube (SI, Figures S25−S28). Higher-purity OAm (98%) was initially used for GC experiments, however when technical grade OAm (40%) was tested, the results were the same. All reactions involving Ge iodides or I_2 or Br_2 with OAm evolve H_2 gas. For larger injections of the headspace, NH_3 gas was also detected, confirmed by the injection of pure ammonia gas to the column as the reference (SI, Figure S26a). The release of NH_3 is consistent with the OAm dimerization fragment observed in HRMS data. To understand how the gas is being formed, reactions of GeI_2 alone or in the presence of Br_2 or I_2 in OAm were performed and all show the presence of H_2 (g). Although the GC performed in this work is not quantitative, the volume of the headspace of each reaction vessel injected into the GC column was held constant. Therefore, higher hydrogen gas intensity for the reactions carried out with GeI_2 and I_2, compared to GeI_2 and Br_2 or GeI_2 alone, was concluded (SI,

DOI: 10.1021/acs.chemmater.9b02225
Chem. Mater. 2019, 31, 7510−7521

Figure S27). It was first presumed that halogen cleaves homolytically and would readily react with the alkene functional group of OAm through the well-known radical mechanism. To further separate the reactivity of the two functional groups of OAm, octylamine (NC_8H_{19}) and 1-octadecene ($C_{18}H_{36}$) were heated separately with I_2, and in all cases, H_2 was detected (SI, Figure S28). This could be from the dehydrogenation reaction of the amines. These reactions are all performed in a closed container so that the H_2 in the headspace provides a reducing environment, but it is not clear if it has a role in the reaction in the solution.[51] Tertiary amines are not able to reduce GeI_2 at the investigated temperature, and the presence of hydrogen on the nitrogen or H_2 (g) formation seem critical for the successful reduction.

As shown in Figure 10, when I_2, GeI_2, or GeI_4 is initially dissolved in degassed OAm (98%), there is a downfield shift

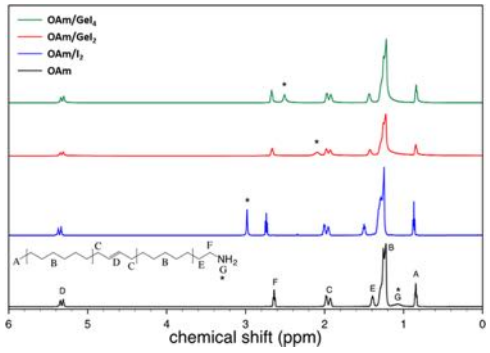

Figure 10. ^{1}H NMR spectra for OAm (98%, degassed, black) and mixtures of OAm and I_2 (blue), OAm and GeI_2 (red), OAm and GeI_4 (green). The * indicates the labile protons on nitrogen, NH_2, NH_3^+.

for the amine protons and the α and β methylene protons in the ^{1}H NMR spectra. In all cases, the chemical shift moves downfield but the magnitude of the shift is dependent on I^-/I_2 concentration.[94,95] These results are consistent with the interaction of sulfur and octylamine, where the amine protons shift as a function of sulfur concentration, which is correlated to the degree of protonation.[101] When I_2 and OAm are left to mix overnight, the downfield shifts increase indicating a higher degree of protonation and a change in the chemical environment due to interaction with I_2 (SI, Figure S30). When OAm and I_2 are heated together under the same reaction conditions, the amine protons are assigned to the peak at 1.86 ppm (2H), and the α and β methylene protons return to their original chemical shifts. As a function of time, the chemical shifts will move downfield, but after a heat treatment, they return close to the original shifts of the solvents. This indicates that the ammonium complex is participating in the reaction.

OAm was first considered since it was shown to be a good solvent, reducing agent, and ligand,[36] but to probe the role of the amine protons in the reaction, DOA and TOA were also investigated. Iodine was left overnight in the presence of OAm, DOA, or TOA, and room temperature NMR in $CDCl_3$ was taken on the resulting mixtures. There are characteristic peaks for the hydrocarbon chains on the various ligands, but for OAm and DOA, the expected amine protons are not present at ~1.0 ppm, and TOA is a tertiary amine and has no proton on nitrogen (Figure 11 and Table S5). The NMR showed a distinct singlet downfield for OAm and DOA, but no difference

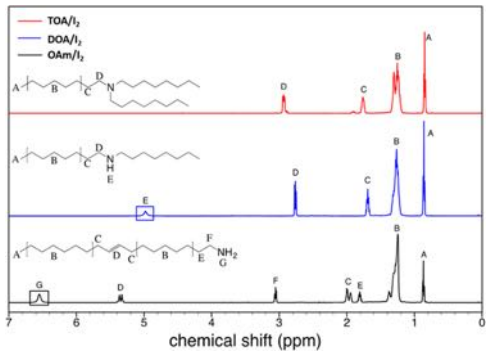

Figure 11. ^{1}H NMR spectra for mixtures of OAm (98%) and I_2, DOA and I_2, and TOA and I_2 after mixing overnight.

for TOA, confirming that the I_2 interacts more strongly with the amine protons. The OAm spectrum has one additional peak at 6.55 ppm, which by integration corresponds to 3H. This is assigned to the protonated iodoamine RNH_3I. Similarly, the extra peak in the DOA spectrum at 4.98 ppm corresponds to 2H and is assigned as R_2NH_2I. This is the evidence for the ammonium iodide complex formed upon the dissolution of the precursors in the solution where the amine and iodine can be considered to be electron donor–acceptor complexes.[102] The amine protons are also required for the formation of the Ge–amine–iodide mixed-ligand complexes.

5. CONCLUDING REMARKS

We have demonstrated that halogens (Br_2 and I_2) can be utilized as a size control agent in the preparation of Ge NCs and that the reduction of Ge halides in OAm occurs with the production of hydrogen and the formation of a Ge–amine–iodide complex. The addition of halogen oxidizes GeI_2 to GeI_4 in situ and provides a finer absolute size control and higher crystallinity as compared to GeI_2/GeI_4 reactions. Halogens facilitate the rapid and efficient microwave heating to produce highly crystalline colloidal nanoparticles. We find that the presence of hydrogen on amine nitrogen is required for the formation of Ge NCs. H_2 and NH_3 gases were observed to be generated in reactions of GeI_2 with amine. I_2 was shown to form Ge–amine–iodide complexes in the solution with primary and secondary amines and to facilitate the formation of H_2 gas. NMR and HRMS confirm that ammonium iodide complexes are present and participate in the mechanism of the Ge NC formation. No imine or nitrile species were detected by FTIR and NMR spectroscopy methods suggesting that the mechanism invoking those species outlined in noble-metal nanoparticle synthesis is not consistent with the formation of Ge NCs. These results toward the mechanistic elucidation of Ge NCs formation in OAm open new routes to a more extensive study of the role of alkylamine organic ligands in the synthesis of nanomaterials.

■ ASSOCIATED CONTENT

Supporting Information

The Supporting Information is available free of charge on the ACS Publications website at DOI: 10.1021/acs.chemmater.9b02225.

PXRD, SAED patterns, microwave temperature profiles, TEM images, size distribution histograms, EDS spectra, solution color pictures, Raman spectra, their fitting

DOI: 10.1021/acs.chemmater.9b02225
Chem. Mater. 2019, 31, 7510–7521

spectra and fitting table, UV−vis−NIR, FTIR, HRMS, GC, and ^{1}H NMR spectra are provided (PDF)

AUTHOR INFORMATION

Corresponding Author

*E-mail: smkauzlarich@ucdavis.edu.

ORCID

Kathryn A. Newton: 0000-0001-6117-4598

Susan M. Kauzlarich: 0000-0002-3627-237X

Notes

The authors declare no competing financial interest.

ACKNOWLEDGMENTS

This work was supported by the National Science Foundation (CHE-1026672, DMR-1035468, CHE-1710110). We thank Prof. Richard Blair (University of Central Florida) for providing phase-pure Ge(II) iodide. We thank Prof. Louise Berben (UC Davis) for the use of the gas chromatograph and Natalia Loewen for assistance with the measurements. We acknowledge the NEAT ORU Keck Spectral Imaging Facility for the use of their laser Raman microscope, the Advanced Materials and Characterization Laboratory (AMCaT) for the use of the Transmission Electron Microscope, and the Mass Spectrometry Facility. We thank Dr William Jewell for helpful discussions.

REFERENCES

(1) Kovalenko, M. V.; Manna, L.; Cabot, A.; Hens, Z.; Talapin, D. V.; Kagan, C. R.; Klimov, V. I.; Rogach, A. L.; Reiss, P.; Milliron, D. J.; et al. Prospects of Nanoscience with Nanocrystals. *ACS Nano* **2015**, *9*, 1012−1057.

(2) Murray, C. B.; Norris, D. J.; Bawendi, M. G. Synthesis and Characterization of Nearly Monodisperse CdE (E = S, Se, Te) Semiconductor Nanocrystallites. *J. Am. Chem. Soc.* **1993**, *115*, 8706−8715.

(3) Cushing, B. L.; Kolesnichenko, V. L.; O'Connor, C. J. Recent Advances in the Liquid-Phase Syntheses of Inorganic Nanoparticles. *Chem. Rev.* **2004**, *104*, 3893−3946.

(4) Bae, W. K.; Joo, J.; Padilha, L. A.; Won, J.; Lee, D. C.; Lin, Q.; Koh, W. K.; Luo, H.; Klimov, V. I.; Pietryga, J. M. Highly Effective Surface Passivation of Pbse Quantum Dots through Reaction with Molecular Chlorine. *J. Am. Chem. Soc.* **2012**, *134*, 20160−20168.

(5) Alivisatos, A. P.; Owen, J. S.; Park, J.; Trudeau, P.-E. Reaction Chemistry and Ligand Exchange at Cadmium−Selenide Nanocrystal Surfaces. *J. Am. Chem. Soc.* **2008**, *130*, 12279−12281.

(6) Lohse, S. E.; Burrows, N. D.; Scarabelli, L.; Liz-Marzán, L. M.; Murphy, C. J. Anisotropic Noble Metal Nanocrystal Growth: The Role of Halides. *Chem. Mater.* **2014**, *26*, 34−43.

(7) Liu, F.; Ding, C.; Zhang, Y.; Kamisaka, T.; Zhao, Q.; Luther, J. M.; Toyoda, T.; Hayase, S.; Minemoto, T.; Yoshino, K.; et al. GeI 2 Additive for High Optoelectronic Quality CsPbI 3 Quantum Dots and Their Application in Photovoltaic Devices. *Chem. Mater.* **2019**, *31*, 798−807.

(8) Cai, Y.; Wang, H.; Li, Y.; Wang, L.; Lv, Y.; Yang, X.; Xie, R. J. Trimethylsilyl Iodine-Mediated Synthesis of Highly Bright Red-Emitting CsPbI 3 Perovskite Quantum Dots with Significantly Improved Stability. *Chem. Mater.* **2019**, *31*, 881−889.

(9) Chockla, A. M.; Klavetter, K. C.; Mullins, C. B.; Korgel, B. A. Solution-Grown Germanium Nanowire Anodes for Lithium-Ion Batteries. *ACS Appl. Mater. Interfaces* **2012**, *4*, 4658−4664.

(10) Yuan, F. W.; Yang, H. J.; Tuan, H. Y. Alkanethiol-Passivated Ge Nanowires as High-Performance Anode Materials for Lithium-Ion Batteries: The Role of Chemical Surface Functionalization. *ACS Nano* **2012**, *6*, 9932−9942.

(11) Xue, D. J.; Wang, J. J.; Wang, Y. Q.; Xin, S.; Guo, Y. G.; Wan, L. J. Facile Synthesis of Germanium Nanocrystals and Their Application in Organic-Inorganic Hybrid Photodetectors. *Adv. Mater.* **2011**, *23*, 3704−3707.

(12) Holman, Z. C.; Liu, C. Y.; Kortshagen, U. R. Germanium and Silicon Nanocrystal Thin-Film Field-Effect Transistors from Solution. *Nano Lett.* **2010**, *10*, 2661−2666.

(13) Nozik, A. J. Nanoscience and Nanostructures for Photovoltaics and Solar Fuels. *Nano Lett.* **2010**, *10*, 2735−2741.

(14) Snyder, G. J.; Toberer, E. S. Complex Thermoelectric Materials. *Nat. Mater.* **2008**, *7*, 105−114.

(15) Saeed, S.; De Weerd, C.; Stallinga, P.; Spoor, F. C.; Houtepen, A. J.; Siebbeles, L. D. A.; Gregorkiewicz, T. Carrier Multiplication in Germanium Nanocrystals. *Light Sci. Appl.* **2015**, *4*, 1−6.

(16) Vaughn, D. D.; Schaak, R. E. Synthesis, Properties and Applications of Colloidal Germanium and Germanium-Based Nanomaterials. *Chem. Soc. Rev.* **2013**, 2861−2879.

(17) Lide, D. R. *CRC Handbook of Chemistry and Physics: A Ready-Reference Book of Chemical and Physical Data, Special Student Edition*, 72nd ed.; CRC Press: Boca raton, FL, 1993.

(18) Lu, X.; Korgel, B. A.; Johnston, K. P. High Yield of Germanium Nanocrystals Synthesized from Germanium Diiodide in Solution. *Chem. Mater.* **2005**, *17*, 6479−6485.

(19) Barry, S. D.; Yang, Z.; Kelly, J. A.; Henderson, E. J.; Veinot, J. G. C. Synthesis of SixGe1-x Nanocrystals Using Hydrogen Silsesquioxane and Soluble Germanium Diiodide Complexes. *Chem. Mater.* **2011**, *23*, 5096−5103.

(20) Guo, Y.; Rowland, C. E.; Schaller, R. D.; Vela, J. Near-Infrared Photoluminescence Enhancement in Ge/CdS and Ge/ZnS Core/Shell Nanocrystals: Utilizing IV/II-VI Semiconductor Epitaxy. *ACS Nano* **2014**, *8*, 8334−8343.

(21) Klimov, V. I.; Lee, D. C.; Werder, D. J.; Pietryga, J. M.; Schaller, R. D.; Robel, I. Colloidal Synthesis of Infrared-Emitting Germanium Nanocrystals. *J. Am. Chem. Soc.* **2009**, *131*, 3436−3437.

(22) Prabakar, S.; Shiohara, A.; Hanada, S.; Fujioka, K.; Yamamoto, K.; Tilley, R. D. Size Controlled Synthesis of Germanium Nanocrystals by Hydride Reducing Agents and Their Biological Applications. *Chem. Mater.* **2010**, *22*, 482−486.

(23) Bernard, A.; Zhang, K.; Larson, D.; Tabatabaei, K.; Kauzlarich, S. M. Solvent Effects on Growth, Crystallinity, and Surface Bonding of Ge Nanoparticles. *Inorg. Chem.* **2018**, *57*, 5299−5306.

(24) Jana, N. R.; Peng, X. Single-Phase and Gram-Scale Routes toward Nearly Monodisperse Au and Other Noble Metal Nanocrystals. *J. Am. Chem. Soc.* **2003**, *125*, 14280−14281.

(25) Sun, S.; Murray, C. B.; Weller, D.; Folks, L.; Moser, A. Monodisperse FePt Nanoparticles and Ferromagnetic FePt Nanocrystal Superlattices. *Science* **2000**, *287*, 1989−1993.

(26) Akkerman, Q. A.; Motti, S. G.; Ram, A.; Kandada, S.; Mosconi, E.; Innocenzo, V. D.; Bertoni, G.; Marras, S.; Kamino, B. A.; Miranda, L.; et al. Solution Synthesis Approach to Colloidal Cesium Lead Halide. *J. Am. Chem. Soc.* **2016**, *138*, 1010−1016.

(27) Protesescu, L.; Yakunin, S.; Bodnarchuk, M. I.; Krieg, F.; Caputo, R.; Hendon, C. H.; Yang, R. X.; Walsh, A.; Kovalenko, M. V. Nanocrystals of Cesium Lead Halide Perovskites (CsPbX3, X = Cl, Br, and I): Novel Optoelectronic Materials Showing Bright Emission with Wide Color Gamut. *Nano Lett.* **2015**, *15*, 3692−3696.

(28) De Roo, J.; Iba, M.; Geiregat, P.; Nedelcu, G.; Walravens, W.; Maes, J.; Martins, J. C.; Van Driessche, I.; Kovalenko, M. V.; Hens, Z. Highly Dynamic Ligand Binding and Light Absorption Coe Ffi Cient of Cesium Lead Bromide Perovskite Nanocrystals. *ACS Nano* **2016**, *10*, 2071−2081.

(29) Joo, J.; Na, H.; Yu, T.; Yu, J. H.; Kim, Y. W.; Wu, F.; Zhang, J. Z.; Hyeon, T. Generalized and Facile Synthesis of Semiconducting Metal Sulfide Nanocrystals. *J. Am. Chem. Soc.* **2016**, *125*, 11100−11105.

(30) Cademartiri, L.; Bertolotti, J.; Sapienza, R.; Wiersma, D. S.; Von Freymann, G.; Ozin, G. A. Multigram Scale, Solventless, and Diffusion-Controlled Route to Highly Monodisperse PbS Nanocrystals. *J. Phys. Chem. B* **2006**, *110*, 671−673.

DOI: 10.1021/acs.chemmater.9b02225
Chem. Mater. 2019, 31, 7510−7521

(31) Cademartiri, L.; Montanari, E.; Calestani, G.; Migliori, A.; Guagliardi, A.; Ozin, G. A.; Giaf, C.; Uni, V.; Usberti, V. G. P.; Parma, I.; et al. Size-Dependent Extinction Coefficients of PbS Quantum Dots. *J. Am. Chem. Soc.* **2006**, *128*, 10337−10346.
(32) Yuan, M.; Kemp, K. W.; Thon, S. M.; Kim, J. Y.; Chou, K. W.; Amassian, A.; Sargent, E. H. High-Performance Quantum-Dot Solids via Elemental Sulfur Synthesis. *Adv. Mater.* **2014**, *26*, 3513−3519.
(33) He, M.; Protesescu, L.; Caputo, R.; Krumeich, F.; Kovalenko, M. V. A General Synthesis Strategy for Monodisperse Metallic and Metalloid Nanoparticles (In, Ga, Bi, Sb, Zn, Cu, Sn, and Their Alloys) via in Situ Formed Metal Long-Chain Amides. *Chem. Mater.* **2015**, *27*, 635−647.
(34) Palomares, V.; Serras, P.; Villaluenga, I.; Hueso, K. B.; Carretero-González, J.; Rojo, T. Na-Ion Batteries, Recent Advances and Present Challenges to Become Low Cost Energy Storage Systems. *Energy Environ. Sci.* **2012**, *5*, 5884−5901.
(35) Larcher, D.; Beattie, S.; Morcrette, M.; Edström, K.; Jumas, J. C.; Tarascon, J. M. Recent Findings and Prospects in the Field of Pure Metals as Negative Electrodes for Li-Ion Batteries. *J. Mater. Chem.* **2007**, *17*, 3759−3772.
(36) Muthuswamy, E.; Iskandar, A. S.; Amador, M. M.; Kauzlarich, S. M. Facile Synthesis of Germanium Nanoparticles with Size Control: Microwave versus Conventional Heating. *Chem. Mater.* **2013**, *25*, 1416−1422.
(37) Ghosh, B.; Ogawara, M.; Sakka, Y.; Shirahata, N. Reductant-Free Colloidal Synthesis of Near-IR Emitting Germanium Nanocrystals: Role of Primary Amine. *J. Nanosci. Nanotechnol.* **2014**, *14*, 2204−2210.
(38) Ruddy, D. A.; Johnson, J. C.; Smith, E. R.; Neale, N. R. Size and Bandgap Control in The. *ACS Nano* **2010**, *4*, 7459−7466.
(39) Muthuswamy, E.; Zhao, J.; Tabatabaei, K.; Amador, M. M.; Holmes, M. A.; Osterloh, F. E.; Kauzlarich, S. M. Thiol-Capped Germanium Nanocrystals: Preparation and Evidence for Quantum Size Effects. *Chem. Mater.* **2014**, *26*, 2138−2146.
(40) Holmes, A. L.; Hütges, J.; Reckmann, A.; Muthuswamy, E.; Meerholz, K.; Kauzlarich, S. M. Probing Electronics as a Function of Size and Surface of Colloidal Germanium Nanocrystals. *J. Phys. Chem. C* **2015**, *119*, 5671−5678.
(41) Ruddy, D. A.; Erslev, P. T.; Habas, S. E.; Seabold, J. A.; Neale, N. R. Surface Chemistry Exchange of Alloyed Germanium Nanocrystals: A Pathway toward Conductive Group IV Nanocrystal Films. *J. Phys. Chem. Lett.* **2013**, *4*, 416−421.
(42) Ramasamy, K.; Kotula, P. G.; Fidler, A. F.; Brumbach, M. T.; Pietryga, J. M.; Ivanov, S. A. SnxGe1-x Alloy Nanocrystals: A First Step toward Solution-Processed Group IV Photovoltaics. *Chem. Mater.* **2015**, *27*, 4640−4649.
(43) Barth, S.; Seifner, M. S.; Bernardi, J. Microwave-Assisted Solution-Liquid-Solid Growth of $Ge_{1-x}Sn_x$ Nanowires with High Tin Content. *Chem. Commun.* **2015**, *51*, 12282−12285.
(44) Esteves, R. J. A.; Ho, M. Q.; Arachchige, I. U. Nanocrystalline Group IV Alloy Semiconductors: Synthesis and Characterization of Ge1- XSnx Quantum Dots for Tunable Bandgaps. *Chem. Mater.* **2015**, *27*, 1559−1568.
(45) Restrepo, D. T.; Lynch, K. E.; Giesler, K.; Kuebler, S. M.; Blair, R. G. Low-Temperature (210 °C) Deposition of Crystalline Germanium via in Situ Disproportionation of GeI 2. *Mater. Res. Bull.* **2012**, *47*, 3484−3488.
(46) *Mathematica 11.0.1.0*; Wolfram Research: Champaign, Illinois, 2016.
(47) Wellner, A.; Paillard, V.; Bonafos, C.; Coffin, H.; Claverie, A.; Schmidt, B.; Heinig, K. H. Stress Measurements of Germanium Nanocrystals Embedded in Silicon Oxide. *J. Appl. Phys.* **2003**, *94*, 5639−5642.
(48) Paillard, V.; Peuch, P.; Laguna, M. A.; Carles, R.; Kohn, B.; Huisken, F. Improved One-Phonon Confinement Model for an Accurate Size Determination of Silicon Nanocrystals. *J. Appl. Phys.* **1999**, *86*, 1921−1924.
(49) Mourdikoudis, S.; Liz-Marzán, L. M. Oleylamine in Nanoparticle Synthesis. *Chem. Mater.* **2013**, *25*, 1465−1476.
(50) Xu, Z.; Shen, C.; Hou, Y.; Gao, H.; Sun, S. Oleylamine as Both Reducing Agent and Stabilizer in a Facile Synthesis of Magnetite Nanoparticles. *Chem. Mater.* **2004**, *21*, 1778−1780.
(51) Chen, M.; Feng, Y. G.; Wang, X.; Li, T. C.; Zhang, J. Y.; Qian, D. J. Silver Nanoparticles Capped by Oleylamine: Formation, Growth, and Self-Organization. *Langmuir* **2007**, *23*, 5296−5304.
(52) Weidman, M. C.; Beck, M. E.; Hoffman, R. S.; Prins, F.; Tisdale, W. A. Nanocrystals via Precursor Stoichiometry Control. *ACS Nano* **2014**, *8*, 6363−6371.
(53) Zhang, J.; Gao, J.; Miller, E. M.; Luther, J. M.; Beard, M. C. Diffusion-Controlled Synthesis of PbS and PbSe Quantum Dots with in Situ Halide Passivation for Quantum Dot Solar Cells. *ACS Nano* **2014**, *8*, 614−622.
(54) Boles, M. A.; Ling, D.; Hyeon, T.; Talapin, D. V. The Surface Science of Nanocrystals. *Nat. Mater.* **2016**, *15*, 141−153.
(55) He, M.; Protesescu, L.; Caputo, R.; Krumeich, F.; Kovalenko, M. V. A General Synthesis Strategy for Monodisperse Metallic and Metalloid Nanoparticles (In, Ga, Bi, Sb, Zn, Cu, Sn, and Their Alloys) via in Situ Formed Metal Long-Chain Amides. *Chem. Mater.* **2015**, *27*, 635−647.
(56) Baghbanzadeh, M.; Carbone, L.; Cozzoli, P. D.; Kappe, C. O. Microwave-Assisted Synthesis of Colloidal Inorganic Nanocrystals. *Angew. Chem., Int. Ed.* **2011**, *50*, 11312−11359.
(57) Kitchen, H. J.; Vallance, S. R.; Kennedy, J. L.; Tapia-Ruiz, N.; Carassiti, L.; Harrison, A.; Whittaker, A. G.; Drysdale, T. D.; Kingman, S. W.; Gregory, D. H. Modern Microwave Methods in Solid-State Inorganic Materials Chemistry: From Fundamentals to Manufacturing. *Chem. Rev.* **2014**, *114*, 1170−1206.
(58) Gabriel, C.; Gabriel, S.; Grant, E. H.; Halstead, B. S. J.; Mingos, M. P. Dielectric Parameters Relevant to Microwave Dielectric Heating. *Chem. Soc. Rev.* **1998**, *27*, 213−223.
(59) Mingos, D. M. P.; Baghurst, D. R. Tilden Lecture: Applications of Microwave Dielectric Heating Effects to Synthetic Problems in Chemistry. *Chem. Soc. Rev.* **1991**, *20*, 1−47.
(60) Bilecka, I.; Niederberger, M. Microwave Chemistry for Inorganic Nanomaterials Synthesis. *Nanoscale* **2010**, *2*, 1358−1374.
(61) Polshettiwar, V.; Nadagouda, M. N.; Varma, R. S. Microwave-Assisted Chemistry: A Rapid and Sustainable Route to Synthesis of Organics and Nanomaterials. *Aust. J. Chem.* **2009**, *62*, 16−21.
(62) Tsuji, M.; Hashimoto, M.; Nishizawa, Y.; Kubokawa, M.; Tsuji, T. Microwave-Assisted Synthesis of Metallic Nanostructures in Solution. *Chem. - Eur. J.* **2005**, *11*, 440−452.
(63) Scherrer, P. Bestimmung Der Groesse Und Der Inneren Struktur Von Kolloidteilchen Mittles Roentgenstrahlen. *Nach. Ges. Wiss* **1918**, *26*, 98−100.
(64) Borchert, H.; Shevchenko, E. V.; Robert, A.; Mekis, I.; Kornowski, A.; Grübel, G.; Weller, H. Determination of Nanocrystal Sizes: A Comparison of TEM, SAXS, and XRD Studies of Highly Monodisperse $CoPt_3$ Particles. *Langmuir* **2005**, *21*, 1931−1936.
(65) Gorokhov, E. B.; Volodin, V. A.; Marin, D. V.; Orekhov, D. A.; Cherkov, A. G.; Gutakovski, A. K.; Shvets, V. A.; Borisov, A. G.; Efremov, M. D. Effect of Quantum Confinement on Optical Properties of Ge Nanocrystals in GeO_2 Films. *Semiconductors* **2005**, *39*, 1168−1175.
(66) Schlecht, S.; Yosef, M.; Fröba, M. Synthesis and Raman Spectroscopy of Nanoparticles of Crystalline and X-Ray Amorphous Germanium within Mesoporous SiO_2. *Z. Anorg. Allg. Chem.* **2004**, *630*, 864−868.
(67) Fukata, N.; Sato, K.; Mitome, M.; Bando, Y.; Sekiguchi, S.; Kirkham, M.; Hong, J.-I.; Wang, Z.; Snyder, R. L. Doping and Raman Characterization of Boron and Phosphorous Atoms in Ge Nanowires. *ACS Nano* **2010**, *4*, 3807−3816.
(68) Ma, X.; Wu, F.; Kauzlarich, S. M. Alkyl-Terminated Crystalline Ge Nanoparticles Prepared from NaGe: Synthesis, Functionalization and Optical Properties. *J. Solid State Chem.* **2008**, *181*, 1628−1633.
(69) Lannin, J. S.; Maley, N. Raman Scattering and Short Range Order in Amorphous Germanium. *Solid State Commun.* **1985**, *53*, 939−942.

DOI: 10.1021/acs.chemmater.9b02225
Chem. Mater. 2019, 31, 7510−7521

(70) Kanakaraju, S.; Sood, A. K.; Mohan, S. In Situ Raman Monitoring of Ultrathin Ge Films. *J. Appl. Phys.* **1998**, *84*, 5756−5760.
(71) Takeuchi, K.; Kosemura, D.; Yokogawa, R.; Usuda, K.; Ogura, A. Origin of Additional Broad Peaks in Raman Spectra from Thin Germanium-Rich Silicon-Germanium Films. *Appl. Phys. Express* **2016**, *9*, No. 071301.
(72) Pescara, B.; Mazzio, K. A.; Lips, K.; Raoux, S. Crystallinity and Size Control of Colloidal Germanium Nanoparticles from Organogermanium Halide Reagents. *Inorg. Chem.* **2019**, *58*, 4802−4811.
(73) Corsini, N. R. C.; Zhang, Y.; Little, W. R.; Karatutlu, A.; Ersoy, O.; Haynes, P. D.; Molteni, C.; Hine, N. D. M.; Hernandez, I.; Gonzalez, J.; et al. Pressure-Induced Amorphization and a New High Density Amorphous Metallic Phase in Matrix-Free Ge Nanoparticles. *Nano Lett.* **2015**, *15*, 7334−7340.
(74) Micoulaut, M.; Cormier, L.; Henderson, G. S. The Structure of Amorphous, Crystalline and Liquid GeO_2. *J. Phys.: Condens. Matter* **2006**, *18*, 753−784.
(75) Pizzagalli, L.; Galli, G. Surface Reconstruction Effects on Atomic Properties of Semiconducting Nanoparticles. *Mater. Sci. Eng., B* **2002**, *96*, 86−89.
(76) Volodin, V. A.; Marin, D. V.; Sachkov, V. A.; Gorokhov, E. B.; Rinnert, H.; Vergnat, M. Applying an Improved Phonon Confinement Model To the Analysis of Raman Spectra of Germanium Nanocrystals. *J. Exp. Theor. Phys.* **2014**, *118*, 65−71.
(77) Hessel, C. M.; Wei, J.; Reid, D.; Fujii, H.; Downer, M. C.; Korgel, B. A. Raman Spectroscopy of Oxide-Embedded and Ligand-Stabilized Silicon Nanocrystals. *J. Phys. Chem. Lett.* **2012**, *3*, 1089−1093.
(78) Gassenq, A.; Milord, L.; Aubin, J.; Pauc, N.; Guilloy, K.; Rothman, J.; Rouchon, D.; Chelnokov, A.; Hartmann, J. M.; Reboud, V.; et al. Raman Spectral Shift versus Strain and Composition in GeSn Layers with 6%-15% Sn Content. *Appl. Phys. Lett.* **2017**, *110*, 112101−15.
(79) Kasper, E.; Perova, T. S.; Schulze, J.; Oehme, M.; Cherevkov, S. Features of Polarized Raman Spectra for Homogeneous and Non-Homogeneous Compressively Strained Ge_{1-y} Sn_y Alloys. *J. Raman Spectrosc.* **2017**, *48*, 993−1001.
(80) Deb, S. K.; Dong, J.; Hubert, H.; McMillan, P. F.; Sankey, O. F. Raman Spectra of the Hexagonal and Cubic (Spinel) Forms of Ge_3N_4: An Experimental and Theoretical Study. *Solid State Commun.* **2000**, *114*, 137−142.
(81) Soignard, E.; McMillan, P. P.; Leinenweber, K. Solid Solutions and Ternary Compound Formation among Ge_3N_4-Si_3N_4 Nitride Spinels Synthesized at High Pressure and High Temperature. *Chem. Mater.* **2004**, *16*, 5344−5349.
(82) Lappert, M. F.; Power, P. P.; Sanger, A. R.; Srivastava, R. C. *Metal and Metalloid Amides*; Ellis Harwood: Chichester, England, 1980.
(83) Jana, N. R.; Peng, X. Single-Phase and Gram-Scale Routes toward Nearly Monodisperse Au and Other Noble Metal Nanocrystals. *J. Am. Chem. Soc.* **2003**, *125*, 14280−14281.
(84) Hiramatsu, H.; Osterloh, F. E. A Simple Large-Scale Synthesis of Nearly Monodisperse Gold and Silver Nanoparticles with Adjustable Sizes and with Exchangeable Surfactants. *Chem. Mater.* **2004**, *16*, 2509−2511.
(85) Vivien, A. Role of Oleylamine Revisited: An Original Disproportionation Route to Monodispersed Cobalt and Nickel Nanocrystals. *Chem. Mater.* **2019**, *31*, 960−968.
(86) Mishra, T.; Sahu, R. K.; Lim, S. H.; Salamanca-Riba, L. G.; Bhattacharjee, S. Hexadecylamine Capped Silver and Gold Nanoparticles: Comparative Study on Formation and Self-Organization. *Mater. Chem. Phys.* **2010**, *123*, 540−545.
(87) Douglass, C. R.; Lynch, M. J.; Jonas, D. M.; Curtis, A. C.; Mateo-Tejada, A. M.; Baranov, D.; Carollo, A. R. Purification of Oleylamine for Materials Synthesis and Spectroscopic Diagnostics for Trans Isomers. *Chem. Mater.* **2019**, *31*, 1223−1230.
(88) Grivas, J. C.; Taurins, A. Reaction of Trichloroacetonitrile With Primary and Seconadry Amines. *Can. J. Chem* **1958**, *37*, 771−774.
(89) Stuart, B. *Infrared Spectroscopy: Fundamentals and Applications*; John Sons, Ltd.: Chichester: U.K., 2004.
(90) Yada, H.; Tanaka, J.; Nagakura, S. Charge-Transfer Complexes between Iodine and Various Aliphatic Amines. *Bull. Chem. Soc. Jpn.* **1960**, *33*, 1661−1667.
(91) Nagakura, S. Molecular Complexes and Their Spectra. VIII. The Molecular Complex between Iodine and Triethylamine. *J. Am. Chem. Soc.* **1958**, *80*, 520−524.
(92) Kobinata, S.; Nagakura, S. Dipole Moments of Charge-Transfer Complexes between Iodine and Some Aliphatic Amines. *J. Am. Chem. Soc.* **1966**, *88*, 3905−3909.
(93) Schug, J. C.; Chang, W. M.; Dyson, M. C. Amine-Iodine Interactions. *Spectrochim. Acta, Part A* **1972**, *28*, 1157−1165.
(94) Schug, J. C.; Chang, W. M.; Kogan, M. J. Iodine-Induced Proton Chemical Shifts in Butyl Amines. *J. Magn. Reson.* **1971**, *4*, 25−29.
(95) Schug, J. C.; Kogan, M. J. The Nature of Iodine-Amine Solutions. *J. Magn. Reson.* **1973**, *11*, 406−415.
(96) Shono, T.; Matsumura, Y.; Inoue, K. Indirect Electrooxidation of Amines to Nitriles Using Halogen Ions as Mediators. *J. Am. Chem. Soc* **1984**, *106*, 6075−6076.
(97) McAlpine, R. K. The Reaction of Dilute Iodine and Ammonia Solutions. *J. Am. Chem. Soc.* **1952**, *74*, 725−727.
(98) Stowell, J. C. 1,2-Diazetidinediones. *J. Org. Chem.* **1967**, *32*, 2360−2362.
(99) Laurence, C.; Graton, J.; Berthelot, M.; El Ghomari, M. J. The Diiodine Basicity Scale: Toward a General Halogen-Bond Basicity Scale. *Chem. - Eur. J.* **2011**, *17*, 10431−10444.
(100) Haynes, W. M. Dissociation Constants of Organic Acids and Bases. In *Handbook of Chemistry and Physics*, 96th ed.; CRC Press, 2015−2016.
(101) Thomson, J. W.; Nagashima, K.; Macdonald, P. M.; Ozin, G. A. From Sulfur-Amine Solutions to Metal Sulfide Nanocrystals: Peering into the Oleylamine-Sulfur Black Box. *J. Am. Chem. Soc* **2011**, *133*, 5036−5041.
(102) Cheng, F.; Davis, M. F.; Hector, A. L.; Levason, W.; Reid, G.; Webster, M.; Zhang, W. Synthesis, Spectroscopic and Structural Systematics of Complexes of Germanium(IV) Halides (GeX4, X = F, Cl, Br or I) with Mono-, Bi- and Tri-Dentate and Macrocyclic Nitrogen Donor Ligands. *Eur. J. Inorg. Chem.* **2007**, *31*, 4897−4905.

DOI: 10.1021/acs.chemmater.9b02225
Chem. Mater. 2019, 31, 7510−7521